Soft Matter

Directed assembly of small binary clusters of magnetizable ellipsoids

Journal:	*Soft Matter*
Manuscript ID	SM-ART-03-2024-000300.R2
Article Type:	Paper
Date Submitted by the Author:	02-Jul-2024
Complete List of Authors:	Harris, David; The University of Alabama in Huntsville Torres-Diaz, Isaac; The University of Alabama in Huntsville

SCHOLARONE™
Manuscripts

Directed assembly of small binary clusters of magnetizable ellipsoids[†]

David H. Harris,[a] and Isaac Torres-Díaz[a*]

We report the effect of shape anisotropy and material properties on the directed assembly of binary suspensions composed of magnetizable ellipsoids. In a Monte Carlo simulation, we implement the ellipsoid-dipole model to calculate the pairwise dipolar interaction energy as a function of position and orientation. The analysis explores dilute suspensions of paramagnetic and diamagnetic ellipsoids with different aspect ratios in a superparamagnetic medium. We analyze the local order of binary structuresas a function of particle aspect ratio, medium permeability, and dipolar interaction strength. Our results show that local order and symmetry are tunable under the influence of a uniform magnetic field when one component of the structure is dilute with respect to the other. The simulation results match previously reported experiments on the directed assembly of binary suspension of spheres. Additionally, we report the conditions on particle aspect ratios and medium properties for various structures with rotational symmetries, as well as open and enclosed structures under the influence of a uniform magnetic field.

1 Introduction

Colloidal particles with surface and shape anisotropy are the focus of intensive research because of their positional and orientational interactions under different field conditions.[1–5] Anisotropic colloids are attractive for different applications, such as microrobots,[6,7] smart materials,[8–10] drug delivery,[11–13] photonics,[14–17] superhydrophobic surfaces,[18–20] and building blocks for colloidal crystals,[21–23] among others. Directed assembly tunes the particle-field and particle-particle interactions to facilitate the formation of different structures.[24–26] Furthermore, directed assembly promotes order and symmetry between particles, resulting in various two and three-dimensional structures.[27–29] Monodisperse colloids with small aspect ratios assemble into close-packed structures,[30–32] intricate chains,[33,34] loops,[35,36] and flower-like structures.[37] Monodisperse magnetizable spheres form head-to-tail chains, bundles of chains, and fibrous structures under the influence of a uniform magnetic field.[38–43] Moreover, monodisperse magnetizable spheres form body-centered tetragonal (BCT) and hexagonally close-packed (HCP) three-dimensional crystals.[31,42,43] Additionally, while monodisperse magnetizable spheres form hexagonal crystals, binary magnetizable spheres with different sizes form triangular and square lattice crystals in two-dimensional confinement under a uniform magnetic field.[44–46] Conversely, uniaxial ellipsoids with high-aspect ratios assemble with face-to-tail arrangement and close-packed structures under a uniform field.[16,17,47–50] The variety of structures makes it essential to have a quantitative model to predict the behavior of magnetizable ellipsoidal particles with different aspect ratios and material properties.

Previous studies show that material properties, relative dimensions, and aspect ratios of colloidal particles directly affect the order of assembled magnetizable particles.[38–40,51–53] Contrary to the aforementioned results in monodisperse suspensions, the directed assembly of binary suspensions composed of paramagnetic and diamagnetic spheres in a ferrofluid medium form structures with rotational symmetry around the particle poles or equator.[27,28] The symmetry of the structures depends on the particle size and their relative polarizations, while their order depends on the relative concentration of their spherical components.[27,28,54] Theoretical studies focus on suspensions composed of spheres with different sizes and material properties. Still, the effect of the shape anisotropy and the dipolar interaction on the order and symmetry of structures has not been fully

explored.

Previous quantitative studies model the dipolar interaction between uniform particles using the point-dipole approximation,[27,28,38–40] the two-point charges approximation,[52,53,55,56] numerical calculations,[57–62] and the ellipsoid-dipole model.[48] The dipolar interaction energy using the point-dipole model is quantified from the disturbance field of polarizable spherical particles in a uniform field.[40,63,64] However, shape anisotropy modifies the disturbance field, and particles with a non-quadratic surface induce non-uniform fields that are not accounted for in the point-dipole model.[65,66] The two-point charges model approximates the disturbance field of uniaxial particles with high aspect ratios,[52,53,55,56] but not for particles with other aspect ratios, such as spheres, oblate spheroids, and scalene ellipsoids. The dipolar interaction for more complex shapes is numerically calculated using computationally expensive methods,[57–62] which are time-consuming when modeling systems of many particles. Alternatively, the recently developed ellipsoid-dipole model takes into account the effect of shape anisotropy on the particle polarization. The ellipsoid-dipole model is used to quantify the pairwise dipolar interaction energy as a function of position and orientation between monodisperse polarizable ellipsoids and between monodisperse permanently magnetized ellipsoids.[26,48] However, we have not found a model to quantify the dipolar interaction between anisotropic particles with different shapes and material properties as a function of their relative position and orientation.

In this manuscript, we analyze the effect of shape anisotropy and material properties on the local order of assembled binary colloidal structures. For this purpose, we consider a binary suspension composed of particles with different material properties, where the concentration of one component is much smaller than the other. We use a superparamagnetic medium (ferrofluid) to tune the polarization of micron-sized particles in a two-dimensional confinement under the influence of a uniform magnetic field. Additionally, we consider a dilute suspension to isolate the effect of the dipolar interaction between particles to the confinement effects generated at suspensions with higher concentrations. The two-dimensional confinement is our first approach to describe the main features of the assembled structures and their dependence on particle aspect ratio and medium properties, which can be used for later studies in more complex systems, such as three-dimensional assembly and tunable crystal structures. Therefore, to model the directed assembly of small binary clusters, we extend the ellipsoid-dipole model to quantify the pairwise dipolar interaction between ellipsoidal particles as a function of their relative position and orientation. The dipolar interaction energy using the ellipsoid-dipole model is implemented in a Monte Carlo algorithm to analyze binary suspensions of magnetizable ellipsoids in a paramagnetic medium. We analyze the directed assembly of a binary suspension composed of diamagnetic and paramagnetic ellipsoids under the influence of a uniform magnetic field. Furthermore, we analyze conditions such that one of the components is dilute with respect to the other component. The study includes the effects of particle size, particle aspect ratio, medium properties, and dipolar interaction strength on the local order and symmetry of the assembled structures in a two-dimensional confinement.

2 Model

2.1 Monte Carlo simulation

We perform Metropolis Monte Carlo (MC) simulations to quantify the canonical ensemble energy in a two-dimensional confinement with periodic boundary conditions.[67–69] We quantify the pairwise interaction energy of interacting magnetizable ellipsoidal particles with different aspect ratios and material properties as a function of their relative position and orientation. The analysis considers dilute suspensions of hard ellipsoids to avoid confinement effects observed at higher concentrations.[70–72] We consider a binary suspension composed

of magnetizable ellipsoids (paramagnetic and diamagnetic) with different aspect ratios in a ferrofluid medium. The system is composed of about 100 uniform particles of the first component and one particle of the second component with a different aspect ratio and material properties. The number of particles is set based on the particle concentration in a square simulation box with periodic boundary conditions. The total particle concentration (area fraction) is fixed at 0.1. The number of particles and the box size for every simulation is in the Supplementary Information (Tables 2-5). We calculate the energy of the system as

$$U = \sum_I^N U_{df}^I + \sum_{I=1}^N \sum_{J \neq I}^N U_{dd}^{IJ}, \tag{1}$$

where U_{df}^I is the induced dipole-field interaction energy of particle I, and U_{dd}^{IJ} is the pairwise induced dipole-dipole interaction energy between magnetizable particles I and J. We consider hard interaction between particles, *i.e.*, infinite energy when the particles overlap and zero when they don't overlap. The MC algorithm samples different particle positions $\mathbf{x} = (x, y, z)$ and orientations, parameterized with unit quaternions q_0, q_1, q_2, and q_3. Quaternions q_1, and q_2 are equal to zero to limit the particle rotation on the simulation plane. We use the unit quaternions to avoid Gimbal lock by using Euler angles and to generate a singularity-free algorithm to quantify the dipolar interaction at arbitrary orientations between particles.[73] The MC algorithm runs until the energy is equilibrated, which requires at least 10^7 steps and varies for different simulation conditions.

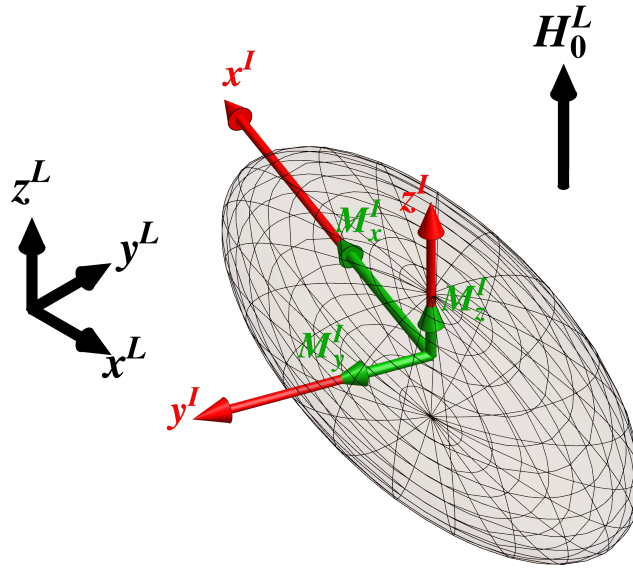## 2.2 Induced dipole – field interaction energy

Fig. 1 Schematic representation of a magnetizable ellipsoidal particle I with an arbitrary position and orientation with respect to the laboratory coordinates (x^L, y^L, z^L), represented in black. The particle coordinate system (x^I, y^I, z^I), in red, is attached to the principal semi-axes of the particle. $\mathbf{H}_0^L$ is the uniform applied field directed along the z^L-axis of the laboratory coordinates. The components (M_x^I, M_y^I, M_z^I) of the induced particle magnetization $\mathbf{M}^I$ are represented in green along the main axes of the particle.

Consider a uniformly magnetizable tri-axial ellipsoidal particle suspended in a uniform isotropic medium, as schematically represented in Figure 1. The particle coordinate system (x^I, y^I, z^I) is colored in red and aligned along the main particle semi-axes r_x, r_y, and r_z. The particle is arbitrarily oriented with respect to laboratory coordinates (x^L, y^L, z^L) and colored in black. The superscript represents the coordinate system where the variable is evaluated. $\mathbf{H}_0^L$ represents the applied uniform magnetic field described in laboratory coordinate, and $\mathbf{M}^I$ is

the magnetization of the particle I described in particle coordinates. The energy of a magnetizable particle in a uniform magnetic field results in[63]

$$u = -\frac{1}{2}\int_{v_p} (\mu_p - \mu_m)\, \mathbf{H}_-^I \cdot \mathbf{H}_0^I \, dv, \tag{2}$$

where v_p is the particle volume, μ_m is the magnetic permeability of the medium, μ_p is the magnetic permeability of the particle, $\mathbf{H}_0^I$ is the applied magnetic field described in particle coordinates, and $\mathbf{H}_-^I$ is the magnetic field inside the particle.

The applied magnetic field described in laboratory coordinates $\mathbf{H}_0^L$ is correlated to the applied magnetic field described in particle I coordinates $\mathbf{H}_0^I$ by

$$\mathbf{H}_0^I = \mathbf{A}^{IL} \cdot \mathbf{H}_0^L, \tag{3}$$

where $\mathbf{A}^{IL}$ is the rotation transformation matrix[73,74]

$$\mathbf{A}^{IL} = \begin{pmatrix} -q_3^2 + q_1^2 - q_2^2 + q_0^2 & 2(q_3 q_0 - q_2 q_1) & 2(q_1 q_3 + q_2 q_0) \\ -2(q_2 q_1 + q_3 q_0) & -q_3^2 - q_1^2 + q_2^2 + q_0^2 & 2(q_1 q_0 - q_2 q_3) \\ 2(q_1 q_3 - q_2 q_0) & -2(q_2 q_3 + q_1 q_0) & q_3^2 - q_1^2 - q_2^2 + q_0^2 \end{pmatrix}, \tag{4}$$

which is defined using unit quaternions q_0, q_1, q_2, and q_3 to parameterize the relative orientation of particle I coordinates with respect to laboratory L coordinates. Unit quaternion parameters and Euler angles are correlated by[73]

$$\begin{aligned} q_0 &= \cos(\phi/2)\cos((\psi+\theta)/2), \\ q_1 &= \sin(\phi/2)\cos((\psi-\theta)/2), \\ q_2 &= \sin(\phi/2)\sin((\psi-\theta)/2), \\ q_3 &= \cos(\phi/2)\sin((\psi+\theta)/2), \end{aligned} \tag{5}$$

where ϕ is the polar angle, θ is the azimuthal angle, ψ is the rotational angle around the z-axis of the particle, and $q_0^2 + q_1^2 + q_2^2 + q_3^2 = 1$. For the two-dimensional analysis, q_1 and q_2 are equal to zero by setting $\phi = \psi = 0$. In Eq. (2), the magnetic field $\mathbf{H}_-^I$ inside the ellipsoidal particle I results in[63]

$$\mathbf{H}_-^I = -\frac{\mu_m H_{0,x}^I \mathbf{e}_x^I}{\mu_m + (\mu_p - \mu_m)\frac{r_x r_y r_z}{2}L_{r_x}(\infty)} - \frac{\mu_m H_{0,y}^I \mathbf{e}_y^I}{\mu_m + (\mu_p - \mu_m)\frac{r_x r_y r_z}{2}L_{r_y}(\infty)} - \frac{\mu_m H_{0,z}^I \mathbf{e}_z^I}{\mu_m + (\mu_p - \mu_m)\frac{r_x r_y r_z}{2}L_{r_z}(\infty)}, \tag{6}$$

where $\mathbf{e}_x^I$, $\mathbf{e}_y^I$, and $\mathbf{e}_z^I$ is a right-handed set of unit vectors along the principal semi-axes of the particle I, $H_{0,j}^I$ is the magnetic field component along the j-axis of the particle I coordinates, and $L_{r_j}(\xi)$ is defined as[48]

$$L_{r_j}(\xi) \equiv \int_0^{\xi} F_{r_j}(\lambda)\,d\lambda, \tag{7}$$

$$F_{r_j}(\lambda) = \frac{1}{\left(\lambda + r_j^2\right)\sqrt{\left(\lambda + r_x^2\right)\left(\lambda + r_y^2\right)\left(\lambda + r_z^2\right)}}, \tag{8}$$

where λ is a dummy variable, and ξ is the ellipsoidal coordinate at the position (x, y, z) with respect to the particle I coordinates, calculated from the real root of

$$\frac{x^2}{r_x^2 + \xi} + \frac{y^2}{r_y^2 + \xi} + \frac{z^2}{r_z^2 + \xi} = 1. \tag{9}$$

The particle magnetization is expressed as $\mathbf{M}^I = \frac{\mu_p - \mu_m}{\mu_0}\mathbf{H}_-^I$, where μ_0 is the vacuum permeability. Eq. (2) reduces

to the induced dipole–field interaction energy of a magnetizable ellipsoidal particle I,

$$U_{df}^I = -\frac{3v_p\mu_m}{2}\left(\mathfrak{f}^I \cdot \mathbf{H}_0^I\right) \cdot \mathbf{H}_0^I, \tag{10}$$

where $v_p = 4\pi r_x r_y r_z/3$ is the particle volume, and $\mathfrak{f}^I$ is the Clausius-Mossotti tensor with a component along the j-axis of the particle I defined as [40,75]

$$\mathfrak{f}_{jj}^I = \frac{1}{3}\frac{(\mu_p - \mu_m)}{\mu_m + (\mu_p - \mu_m)\frac{r_x r_y r_z}{2}L_{r_j}(\infty)}. \tag{11}$$

2.3 Ellipsoid-dipole model for magnetizable ellipsoids

The magnetic scalar potential at the position (x,y,z) outside a magnetizable ellipsoid and relative to the particle coordinates, due to a uniform magnetic field, is quantified by [63]

$$\phi^+ = -\left[\left(\frac{\mu_m + (\mu_p - \mu_m)\frac{r_x r_y r_z}{2}L_{r_x}(\xi)}{\mu_m + (\mu_p - \mu_m)\frac{r_x r_y r_z}{2}L_{r_x}(\infty)}\right)x\,H_{0,x}+\right.$$

$$\left(\frac{\mu_m + (\mu_p - \mu_m)\frac{r_x r_y r_z}{2}L_{r_y}(\xi)}{\mu_m + (\mu_p - \mu_m)\frac{r_x r_y r_z}{2}L_{r_y}(\infty)}\right)y\,H_{0,y}+$$

$$\left.\left(\frac{\mu_m + (\mu_p - \mu_m)\frac{r_x r_y r_z}{2}L_{r_z}(\xi)}{\mu_m + (\mu_p - \mu_m)\frac{r_x r_y r_z}{2}L_{r_z}(\infty)}\right)z\,H_{0,z}\right]. \tag{12}$$

The magnetic field outside the particle ($\xi > 0$) results from the negative gradient of the magnetic potential ϕ^+. After some algebraic manipulation (See Supplementary Information), the disturbance on the uniform magnetic field outside the ellipsoidal particle ($\xi > 0$) results in

$$\mathbf{H}^I = \frac{3r_x r_y r_z}{2}\mathscr{G}^I(\xi)\cdot\mathfrak{f}^I\cdot\mathbf{H}_0^I, \tag{13}$$

where $\mathscr{G}$ is a tensor with components [48]

$$\mathscr{G}_{ij} = \left[\delta_{ij}\left(L_{r_j}(\xi) - L_{r_j}(\infty)\right) + x_j\frac{\partial L_{r_j}(\xi)}{\partial x_i}\right], \tag{14}$$

where δ_{ij} is the identity tensor, $L_{r_j}(\xi)$ is defined in Eq. (7), and $\frac{\partial L_{r_j}(\xi)}{\partial x_i} = \frac{\partial L_{r_j}(\xi)}{\partial \xi}\frac{\partial \xi}{\partial x_i}$, with

$$\frac{\partial L_{r_j}(\xi)}{\partial \xi} = F_{r_j}(\xi), \tag{15}$$

$$\frac{\partial \xi}{\partial x_i} = \frac{2x_i}{(r_i^2+\xi)}\bigg/\left(\frac{x^2}{(r_x^2+\xi)^2} + \frac{y^2}{(r_y^2+\xi)^2} + \frac{z^2}{(r_z^2+\xi)^2}\right). \tag{16}$$

Eq. (13) is denoted as the ellipsoid-dipole model for magnetizable particles and quantifies the disturbance field generated by a magnetizable ellipsoidal particle under the influence of a uniform magnetic field. It is noted that Eq. (13) differs by a factor of three from its equivalent expression for permanently magnetized ellipsoids, [48] which appears due to the definition of the Clausius-Mossotti factor in Eq. (11). [40,75]
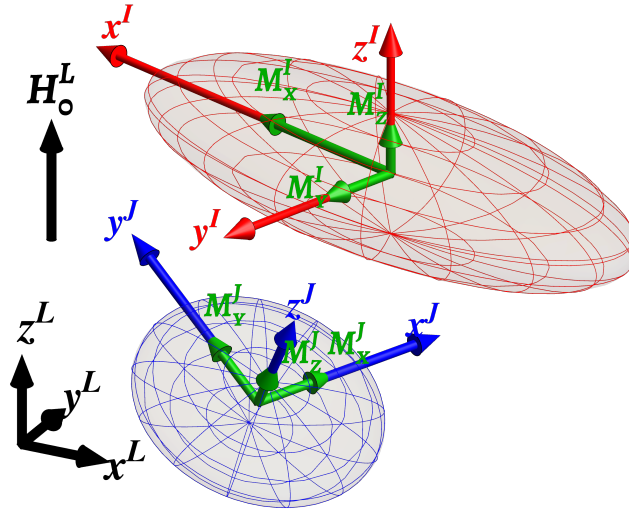
Fig. 2 Schematic representations of two interacting magnetizable ellipsoidal particles under the influence of a uniform magnetic field $\mathbf{H}_0^L$. Both particles are arbitrarily positioned and oriented with respect to the laboratory coordinates. The red coordinate system (x^I, y^I, z^I) is attached to the principal semi-axes of particle I, while the blue coordinate system (x^J, y^J, z^J) is attached to the principal semi-axes of particle J. The components of the induced particle magnetization are represented in green along the main axes of each particle.

2.4 Induced dipole – dipole interaction energy

Consider two magnetizable ellipsoidal particles with arbitrary sizes and aspect ratios under the influence of a uniform magnetic field, as schematically represented in Figure 2. Superscripts I, J, and L stand for the coordinate system where the variable is evaluated. r_x^I, r_y^I, and r_z^I represent the semi-axes of particle I, while r_x^J, r_y^J, and r_z^J represent the semi-axes of particle J. The red coordinate system is attached to the principal semi-axes of particle I. The blue coordinate system is attached to the principal semi-axes of particle J. Both particles have an induced magnetization vector represented by green arrows in their coordinate systems. The particles are arbitrarily positioned and orientated with respect to the laboratory coordinates, where $\mathbf{q}^I$ and $\mathbf{q}^J$ are the quaternion parameters of particles I and J with respect to the laboratory coordinates,[73,74] respectively.

From Eq. (2), the dipolar interaction energy due to the induced dipole field of particle I on the induced dipole of particle J results in

$$U_{dd}^{IJ} = -\frac{3 v_p^J \mu_m}{2} \left(\mathfrak{f}^J \cdot \mathbf{H}_0^J \right) \cdot \mathbf{H}^I, \tag{17}$$

where $\mathbf{H}^I$ is the field generated by the induced dipole of particle I at the position of particle J (Eq. (13)), $\mathbf{H}_0^J$ is the applied magnetic field described in particle J coordinates; $\mathfrak{f}^J$ and v_p^J are the Clausius-Mossotti tensor and the volume of particle J, respectively. Since $\mathbf{H}^I$ and $\left(\mathfrak{f}^J \cdot \mathbf{H}_0^J \right)$ are in different coordinate systems, we use the relative transformation matrix $\mathbf{A}^{JI}$ to transform the field in particle I coordinates into particle J coordinates. The relative quaternions $\mathbf{q}^{IJ}$ between particle I and particle J are calculated by[73]

$$\begin{pmatrix} q_0^{IJ} \\ q_1^{IJ} \\ q_2^{IJ} \\ q_3^{IJ} \end{pmatrix} = \begin{pmatrix} q_0^J & q_1^J & q_2^J & q_3^J \\ -q_1^J & q_0^J & -q_3^J & q_2^J \\ -q_2^J & q_3^J & q_0^J & -q_1^J \\ -q_3^J & -q_2^J & q_1^J & q_0^J \end{pmatrix} \cdot \begin{pmatrix} q_0^I \\ q_1^I \\ q_2^I \\ q_3^I \end{pmatrix}. \tag{18}$$

The relative quaternions are incorporated in Eq. (4) to calculate the relative transformation matrix $\mathbf{A}^{JI} =$

$(\mathbf{A}^{IJ})^{-1}$. Therefore, replacing Eqs. (3) and (13) into Eq. (17), the dipolar interaction energy due to the induced dipole field of particle I on the induced dipole of particle J results in

$$U_{dd}^{IJ} = -\left(\frac{27\mu_m}{16\pi}v_p^J v_p^I\right)\left(\mathfrak{f}^J \cdot \mathbf{H}_0^J\right) \cdot \left(\mathbf{A}^{JI} \cdot \mathscr{G}^I \cdot \mathfrak{f}^I \cdot \mathbf{H}_0^I\right), \tag{19}$$

where $\mathfrak{f}^I$ is defined in Eq. (11). $\mathscr{G}^I$ is defined in Eq. (14) and evaluated at the relative coordinate ξ of particle J with respect to particle I. Similarly, the dipolar interaction energy due to the induced dipole field of particle J on the induced dipole of particle I results in

$$U_{dd}^{JI} = -\left(\frac{27\mu_m}{16\pi}v_p^J v_p^I\right)\left(\mathfrak{f}^I \cdot \mathbf{H}_0^I\right) \cdot \left(\mathbf{A}^{IJ} \cdot \mathscr{G}^J \cdot \mathfrak{f}^J \cdot \mathbf{H}_0^J\right), \tag{20}$$

where $\mathscr{G}^J$ is evaluated at the relative coordinate ξ of particle I with respect to particle J. Therefore, using Eqs. (19) and (20), the pairwise dipolar interaction energy between particles I and J results in

$$U_{dd} = U_{dd}^{IJ} + U_{dd}^{JI}. \tag{21}$$

2.5   Dimensionless parameters

The induced dipole–field interaction energy is characterized by

$$\alpha \equiv \frac{3}{2}\frac{\mu_m v_p \mathfrak{f}_0 H_0^2}{k_B T}, \tag{22}$$

which represents the dimensionless ratio between the magnetic energy and thermal energy, where $\mathfrak{f}_0$ is the maximum absolute component of the Clausius-Mossotti tensor, H_0 is the applied magnetic field strength, v_p represents the particle volume, k_B is the Boltzmann constant, and T is the absolute temperature. The dimensionless induced dipole–field interaction energy $\tilde{U}_{df}^I$ of a magnetizable ellipsoidal particle becomes

$$\tilde{U}_{df}^I = -\alpha\left(\tilde{\mathfrak{f}}^I \cdot \tilde{\mathbf{H}}_0^I\right) \cdot \tilde{\mathbf{H}}_0^I, \tag{23}$$

where $\tilde{\mathfrak{f}}^I = \mathfrak{f}^I/f_0$ is the normalized Clausius-Mossotti tensor of particle I, and $\tilde{\mathbf{H}}_0^I = \mathbf{H}_0^I/H_0$ is the unit vector along the direction of the applied magnetic field described in particle I coordinates. Similarly, using the same characteristic variables, we define the dimensionless induced dipole-dipole interaction parameter,

$$\beta \equiv \frac{9}{4}\frac{v_p^I v_p^J}{v_m}\frac{\mu_m f_0^2 H_0^2}{k_B T}, \tag{24}$$

which represents the ratio between dipolar interaction energy and thermal energy, where $v_m = \frac{4}{3}\pi r_m^3$ represents the volume of a reference spherical particle with a radius r_m equal to the minimum semi-axis of both particles. Therefore, the dimensionless pairwise dipolar interaction energy results in

$$\tilde{U}_{dd} = \tilde{U}_{dd}^{IJ} + \tilde{U}_{dd}^{JI} = -\beta\left(\tilde{\mathfrak{f}}^J \cdot \tilde{\mathbf{H}}_0^J\right) \cdot \left(\mathbf{A}^{JI} \cdot \tilde{\mathscr{G}}^I \cdot \tilde{\mathfrak{f}}^I \cdot \tilde{\mathbf{H}}_0^I\right) - \beta\left(\tilde{\mathfrak{f}}^I \cdot \tilde{\mathbf{H}}_0^I\right) \cdot \left(\mathbf{A}^{IJ} \cdot \tilde{\mathscr{G}}^J \cdot \tilde{\mathfrak{f}}^J \cdot \tilde{\mathbf{H}}_0^J\right), \tag{25}$$

where $\tilde{\mathfrak{f}}^I = \mathfrak{f}^I/\mathfrak{f}_0$ and $\tilde{\mathfrak{f}}^J = \mathfrak{f}^J/\mathfrak{f}_0$ are the normalized Clausius-Mossotti factors of particle I and J, respectively. $\tilde{\mathbf{H}}_0^I = \mathbf{H}_0^I/H_0$ and $\tilde{\mathbf{H}}_0^J = \mathbf{H}_0^J/H_0$ are the unit vectors along the direction of the applied magnetic field, described in particle I and J coordinates, respectively. The tensor $\tilde{\mathscr{G}}^I$ is evaluated at the relative position of particle J with respect to particle I, while $\tilde{\mathscr{G}}^J$ is evaluated at the relative position of particle I with respect to particle J.
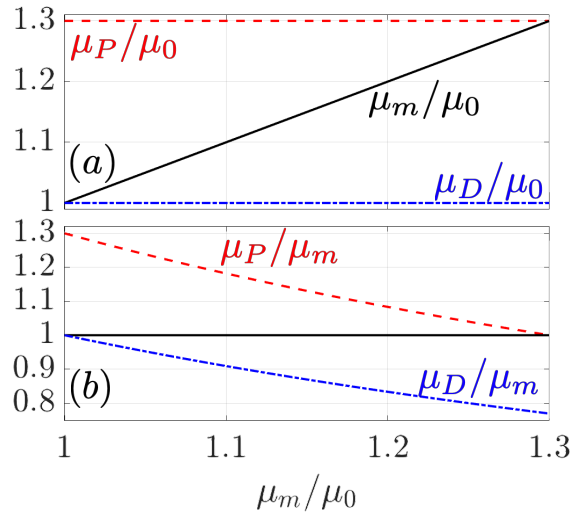
Fig. 3 (a) Variation of medium permeability between the diamagnetic and paramagnetic permeabilities. (b) Relative permeabilities of the diamagnetic and paramagnetic particles with respect to the medium permeability.

The dimensionless parameters α and β change for different particle aspect ratios and sizes, as in the case of binary or polydisperse suspensions. In the present analysis, we use the minimum semi-axes of both particles (r_m) as a characteristic length. Therefore, the dimensionless parameters α and β can be written as

$$\alpha = \alpha_s \left(\tilde{r}_x \tilde{r}_y \tilde{r}_z \right), \tag{26}$$

$$\beta = \frac{3}{2} \mathfrak{f}_0 \alpha_s \left(\tilde{r}_x^I \tilde{r}_y^I \tilde{r}_z^I \right) \left(\tilde{r}_x^J \tilde{r}_y^J \tilde{r}_z^J \right), \tag{27}$$

where $\alpha_s \equiv \frac{2\pi\mu_m r_m^3 \mathfrak{f}_0 H_0^2}{k_B T}$ represents the induced dipole-field interaction parameter of the equivalent sphere with a radius r_m equal to the minimum semi-axis of the particles, and $\tilde{r}_x = r_x/r_m$, $\tilde{r}_y = r_y/r_m$, and $\tilde{r}_z = r_z/r_m$ are the normalized semi-axes of the particle.

2.6 Overlap condition and excluded volume between particles

The overlap condition between hard ellipsoids is based on three levels of approximation extended from the algorithm explained in previous work.[48,76] First, a separation between particles greater than the sum of the radii of the circumscribed spheres around each particle guarantees no particle overlap. Second, we use the distance between a particle surface and the three principal planes of a circumscribed rectangular prism on a neighboring particle.[76,77] The third approximation uses a refined particle mesh to ensure no particle overlap.[76,77] Additionally, we use the recently published methodology to quantify the excluded volume between two ellipsoids.[48]

2.7 Radial distribution function

We calculate the radial distribution function $g(\tilde{r})$ between the central particle and the surrounding satellite particles by

$$g\left(\tilde{\mathbf{r}}\right) = \frac{1}{(N-1)\rho} \left\langle \sum_{J=1, J \neq I}^{N} \delta(\tilde{\mathbf{r}} - \tilde{\mathbf{r}}^{IJ}) \right\rangle, \tag{28}$$

where ρ is the particle density.[68] We calculate the radial distribution function using 2×10^4 steps uniformly distributed over two million steps after the system is equilibrated.

2.8   Simulation conditions

We simulate the directed assembly of binary suspensions composed of paramagnetic (P) and diamagnetic (D) uniaxial ellipsoids with different sizes and aspect ratios suspended in a ferrofluid medium. The aspect ratio of the uniaxial ellipsoid is $\tilde{r}_x/\tilde{r}_y$, where $\tilde{r}_x \geq \tilde{r}_y = \tilde{r}_z$. For the case of spheres ($\tilde{r}_x = \tilde{r}_y = \tilde{r}_z$), we report the normalized particle radius $\tilde{r} = r/r_m$, with $r_m = 1$ μm. We change the aspect ratio $\tilde{r}_x/\tilde{r}_y$ of uniaxial ellipsoids while keeping their minimum axis constant. Additionally, one of the components in the binary suspension is dilute with respect to the second component. The number ratio between diamagnetic and paramagnetic particles (N_D/N_P) is in the order of 100 to guarantee a predicted equilibrium structure around the paramagnetic particle, as shown in Figure S1. The total particle concentration (area fraction) is fixed at 0.1. The number of particles and the box size for every simulation is in the Supplementary Information (Tables 2-4).

In the model validation, we use the same conditions reported in the experiments, with $r_m = 1.35$ μm.[28] The dimensionless radii for the paramagnetic and diamagnetic particles are $\tilde{r}^P = 1$ and $\tilde{r}^D = 3.67$, respectively. Moreover, the magnetic susceptibility of the paramagnetic and diamagnetic particles are $\chi_P = 3$ and $\chi_D = -0.75 \times 10^{-5}$, respectively. The relative permeability of the medium is calculated by[78]

$$\chi_m = \frac{\pi}{18}\phi_f\mu_0\frac{M_d^2 d^3}{k_B T}, \tag{29}$$

where d is the diameter of the magnetic nanoparticle (10 nm), M_d is the domain magnetization (4.46×10^5A/m), and ϕ_f is the volume fraction of the ferrofluid. Using the reported values of $\phi_f = 0.002 - 0.02$,[28] the relative permeability of the medium is in the range between 1.02 to 1.22. Furthermore, replacing in Eq. (22) the reported value of the magnetic field of $\mu_0 H_0 = 60$ gauss,[28] the dipole-field interaction parameters (α_s) result 55×10^3 and 58×10^3 for medium permeabilities 1.02 and 1.22, respectively. Additionally, we analyze the assembly at different fields of 6 and 12 gauss.

The relative permeabilities of the diamagnetic and paramagnetic particles are constants, $\mu_D/\mu_0 = 1$ and $\mu_P/\mu_0 = 1.3$, respectively. The magnetic susceptibility of the paramagnetic spheres varies between 0.19 and 0.75.[79–83] We use a representative magnetic susceptibility value of 0.3 for a paramagnetic sphere ($r_m = 1$ μm). Furthermore, we use the magnetic susceptibility value of diamagnetic polystyrene beads equal to -0.75×10^{-5}.[27,28] We modify the medium permeability between the diamagnetic and paramagnetic values, as shown in Figure 3(a). Therefore, the relative permeability of diamagnetic and paramagnetic particles relative to the ferrofluid medium changes, as depicted in Figure 3(b). Hereafter, we report the results as a function of the relative permeability of the ferrofluid medium. The direction of the applied magnetic field is perpendicular to the assembly plane. We include all N^2 pairs with no cutoff radius to calculate the dipolar interaction between particles. Furthermore, we set the length of the square simulation box larger than the length of the interaction. The box size for every simulation is in the Supplementary Information. Additionally, the induced dipole-field interaction parameter is set at $\alpha_s = 100, 250, 500, 10^3$,and 10^4, while the dipolar interaction parameter β is directly proportional to α_s, as described in Eq. (27).[27,28]

3   Results and Discussion

3.1   Pairwise dipolar interaction of two magnetizable ellipsoids

Figure 4 shows the pairwise dipolar interaction energy between two magnetizable particles with different aspect ratios as a function of the medium permeability μ_m/μ_0. The uniform magnetic field is perpendicular to the plane of analysis. The top panel in Figure 4 represents the relative permeabilities of the particles with respect to the medium permeability, and the markers correspond to the conditions reported in every
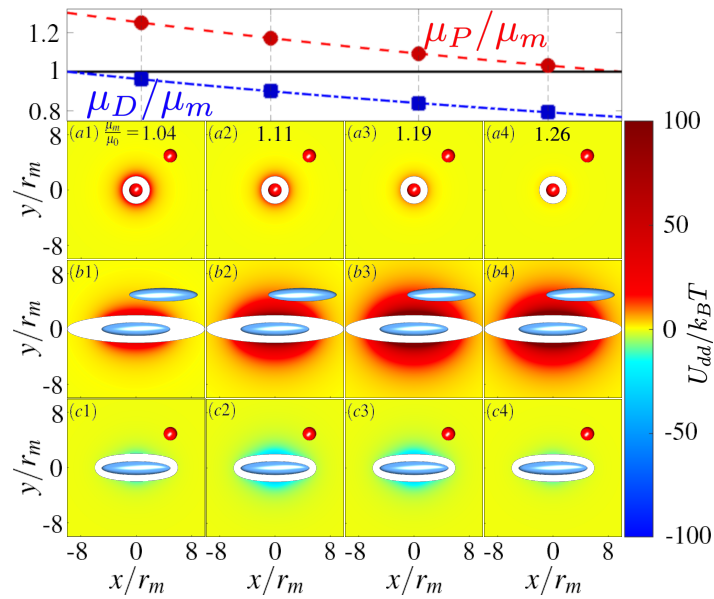
Fig. 4 The induced dipole-dipole interaction energy with a fixed parallel orientation between (a) two paramagnetic spheres $\tilde{r}^P = 1$, (b) two diamagnetic ellipsoids $\tilde{r}_x^D/\tilde{r}_y^D = 5$, and (c) a paramagnetic sphere $\tilde{r}^P = 1$ and a diamagnetic ellipsoid $\tilde{r}_x^D/\tilde{r}_y^D = 5$ as a function of the separation distance between particles and the medium permeability μ_m/μ_0. The pairwise dipolar interaction energy U_{dd} is in $k_B T$ units. The magnetic field is directed perpendicular to the plane. The white region corresponds to the excluded volume between particles for the considered particle orientations.

column. Figure 4(a) shows the dipolar interaction energy between two paramagnetic spheres $\tilde{r}^P = 1$ is repulsive and isotropic on the interaction plane. The magnitude of the dipolar interaction energy decreases with the separation distance and as the medium permeability μ_m/μ_0 increases. Furthermore, since the particle magnetization is parallel to the applied magnetic field in magnetizable spheres, the dipolar interaction energy is not dependent on the relative particle orientation between particles.

Figure 4(b) shows the pairwise dipolar interaction energy between two diamagnetic ellipsoids with aspect ratio $\tilde{r}_x^D/\tilde{r}_y^D = 5$ as a function of the medium permeability. The results show that the maximum dipolar interaction energy is along the minimum axis of the ellipsoid, *i.e.*, along the sides of the ellipsoid. Like Figure 4(a), the dipolar interaction energy vanishes as the separation distance between particles increases. Moreover, the magnitude of the dipolar interaction energy between ellipsoids is one order of magnitude greater than the one between paramagnetic spheres. The difference is due to the proportionality of the interaction energy with particle volume, as described in Eq. (24). Additionally, the dipolar interaction energy increases as the medium permeability increases, reaching a maximum when $\mu_m/\mu_0 = 1.26$.

Figure 4(c) shows the pairwise interaction energy between a paramagnetic sphere $\tilde{r}^P = 1$ and a diamagnetic ellipsoid with aspect ratio $\tilde{r}_x^D/\tilde{r}_y^D = 5$. The results show that the dipolar interaction energy well is located along the sides of the ellipsoid, *i.e.*, the sphere is more probable to be positioned along the side of the ellipsoid. Similar to the previous cases, the interaction energy decreases as the separation distance between particles increases. The dipolar interaction energy trend between a paramagnetic sphere and a diamagnetic ellipsoid differs from the corresponding interaction between the individual components. In this case, the dipolar interaction increases when relative particle permeabilities are in the same order of magnitude, *i.e.*, $\mu_m/\mu_0 = 1.11 - 1.19$, and it decreases when the particle permeability approaches the value of the medium permeability, *i.e.*, $\mu_m/\mu_0 = 1.04$ and 1.26. The dipolar interaction energy between an ellipsoid and a larger
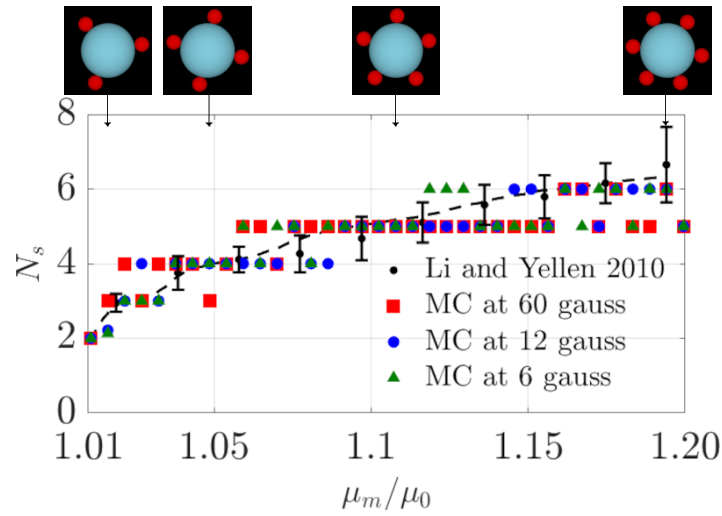
Fig. 5 Average number N_s of paramagnetic spheres in the binary structure as a function of medium permeability. The dashed line and the black dots correspond to the reported experimental results from Ref.[28]. The colored dots represent the results from Monte Carlo (MC) simulations at different magnetic fields. Renderings are shown at the top with the diamagnetic particle (cyan) and the surrounding paramagnetic particles (red) for different medium permeabilities.

paramagnetic sphere follows the same trend as Figure 4(c) but with a larger magnitude (not shown) due to its proportionality with particle volume (Eq. (24)).

3.2 Model Validation

The equilibrium binary structures composed of paramagnetic spheres ($\tilde{r}^P = 1$) around a central diamagnetic sphere ($\tilde{r}^D = 3.67$) for different ferrofluid concentrations were recently reported, showing a tunable orientational symmetry of paramagnetic spheres around the diamagnetic particle.[27,28] We compare the results of MC simulations with previously reported experiments of binary structures (Fig. 2 of Ref.[28]). The simulation conditions for the validation are in Table 1 in the supplementary information. Figure 5 shows the simulation and previous experimental results for the average number of satellite particles (N_s) of binary structures at different medium permeabilities. The simulation results at different applied magnetic fields show a similar trend as a function of the medium permeability compared to the reported experiments in Ref.[28]. Furthermore, Figure S2 shows the radial distribution function $g(\tilde{r})$ between the diamagnetic particle (cyan) and surrounding paramagnetic particles (red) for different medium permeabilities.

Even though the trend of N_s as a function of the medium permeability is similar to the experiments, there is a mismatch between the simulations and experiments, which is attributed to two factors. First, the MC simulations do not consider the electrostatic and van der Waals interactions between particles, which screen the dipolar interaction and reduce the energy well near the central particle. Second, there is no magnetic susceptibility measurement for the ferrofluid dilutions used in the experiments, which might generate a shift in the relative permeability.[28] The dipolar interaction between particles dominates the short-range behavior of $g(\tilde{r})$ at different applied magnetic fields (Figure S2), which results in a similar pattern of N_s to variations of medium permeability. Furthermore, the dipole-field interaction parameter α_s in the experiments results in the order of 5×10^4 for the applied field of $\mu_0 H_0 = 60$ gauss, promoting a long-range interaction between particles. The distance from the central particle where the distribution of paramagnetic spheres becomes isotropic increases as the applied magnetic field increases. To reduce the interaction length between particles in our simulations,
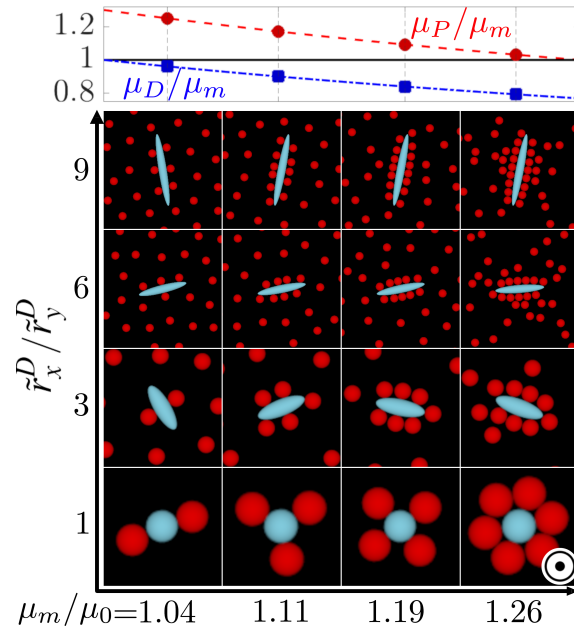
Fig. 6 Snapshots of the Monte Carlo simulations of the directed assembly of binary systems composed of a central diamagnetic ellipsoid with different aspect ratios ($\tilde{r}_x^D/\tilde{r}_y^D$) surrounded by paramagnetic spheres ($\tilde{r}^P = 1$) at $\alpha_s = 10^4$. The representative assembled structures are presented as a function of the relative medium permeability.

we use smaller α_s values, which also produce a similar pattern of the assembled structures, as shown in Figure 5.

3.3   Central Diamagnetic Ellipsoid

First, we will describe the main features of the assembled structures at high α_s values. Then, we will analyze the impact of dipolar interactions on the structures in section 3.6. Figure 6 show snapshots of MC simulations of the directed assembly of a diamagnetic ellipsoid with different aspect ratios ($1 \leq \tilde{r}_x^D/\tilde{r}_y^D \leq 9$) and paramagnetic spheres ($\tilde{r}^P = 1$) as a function of the relative medium permeability μ_m/μ_0. Figure S3 depicts the radial distribution function $g(\tilde{r})$ for different conditions analyzed in Figure 6. The paramagnetic particles, diamagnetic particles, and ferrofluid medium are colored red, cyan, and black, respectively. Hereafter, we will use the same color scheme to represent the particles and medium in the subsequent figures. The top panel in Figure 6 represents the relative permeabilities of the particles with respect to the medium, where the markers correspond to the conditions reported in the snapshots. Simulation results reflect two main patterns of the equilibrium structures. First, increasing the aspect ratio of the diamagnetic ellipsoid breaks the rotational symmetry (fold symmetry) of the paramagnetic spheres around the diamagnetic particle. Second, the number of the assembled paramagnetic spheres around the diamagnetic ellipsoid increases as the medium permeability increases.

In the first pattern, the directed assembly of diamagnetic and paramagnetic spheres ($\tilde{r}^D = \tilde{r}^P = 1$) generates structures with n-fold rotational symmetry around the diamagnetic sphere (Figure 6 - bottom row), tuning the structures from 2-fold to 6-fold symmetry as medium permeability increases. It has the same phenomenological behavior reported in Figure 5. Additionally, Figure 6 shows that as the aspect ratio $\tilde{r}_x^D/\tilde{r}_y^D$ of the ellipsoid increases, the rotational symmetry switches to a two-fold symmetry around the major axis of the diamagnetic ellipsoid. Moreover, increasing the aspect ratio of the diamagnetic ellipsoid increases the number of assembled paramagnetic (satellite) particles.
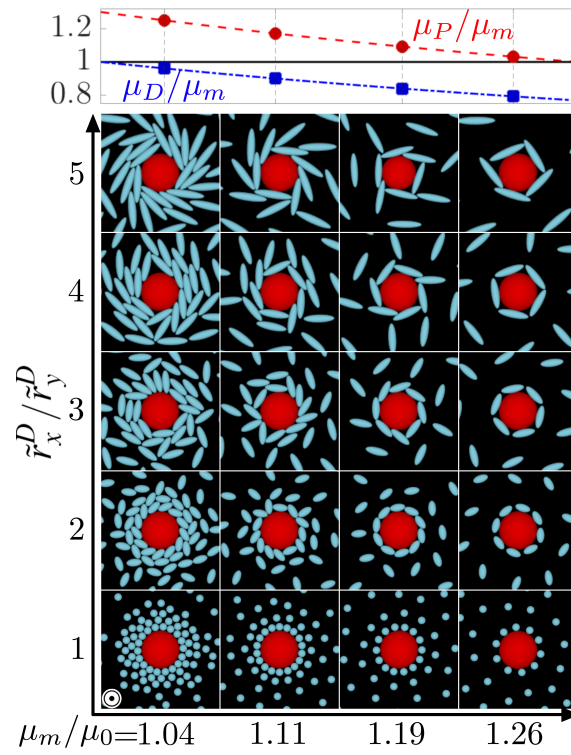
Fig. 7 Snapshots of the Monte Carlo simulations of the directed assembly of binary systems composed of a paramagnetic sphere (red) with radius $\tilde{r}^P = 5$ and diamagnetic ellipsoids (cyan) with different aspect ratios $\tilde{r}^D_x/\tilde{r}^D_y$ at $\alpha_s = 10^4$.

In the second pattern, changing the medium permeability tunes the dipolar interaction (Eq. (25)) and the number of particles in the structure, as shown in every row for different aspect ratios in Figure 6. The relative permeabilities of the paramagnetic and diamagnetic particles decrease as the medium permeability increases. However, the maximum absolute value of the Clausius-Mossotti factor (Eq. (11)) of the paramagnetic particle decreases, while the one of diamagnetic particles increases. Low medium permeabilities promote strong repulsive interactions between paramagnetic particles (Figure 4(a1)), limiting the number of paramagnetic spheres around the diamagnetic particle. However, high medium permeabilities reduce the dipolar interaction between paramagnetic particles (Figure 4(a4)), promoting close-packed configurations of paramagnetic spheres around the diamagnetic particle. Thus, reducing the difference between the paramagnetic particle and medium permeabilities reduces the dipolar interaction between the particles and promotes close-packed structures around the diamagnetic (central) particle.

3.4 Central Paramagnetic Sphere

Figure 7 shows screenshots of MC simulations of the directed assembly of binary suspensions composed of a paramagnetic sphere ($\tilde{r}^P = 5$) and diamagnetic (satellite) ellipsoids with aspect ratio $1 \leq \tilde{r}^D_x/\gamma^D_y \leq 5$. Furthermore, Figure S4 depicts the radial distribution function $g(\tilde{r})$ for different conditions analyzed in Figure 7. The phenomenological behavior of the assembled structures is opposite to what Figure 6 shows. Simulation results in Figure 7 show that the orientational symmetry of the diamagnetic ellipsoids around the paramagnetic sphere increases as the medium permeability increases. Additionally, the rotational symmetry breaks down as the aspect ratio of the diamagnetic particles increases and the medium permeability decreases. Both patterns are correlated to the dipolar interaction (Figure 4) and packing arrangement between particles, as explained below.
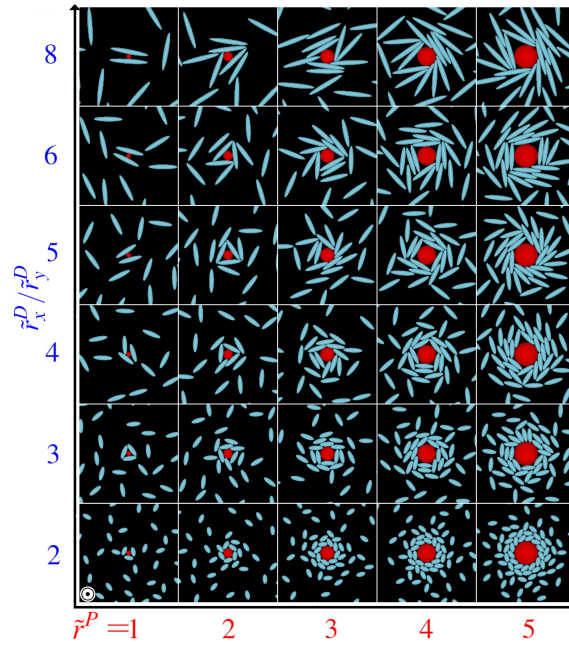
Fig. 8 Snapshots of the Monte Carlo simulations of the directed assembly of binary suspensions composed of a paramagnetic sphere (red) with radius $\tilde{r}^P$ and diamagnetic ellipsoids (cyan) with different aspect ratios $\tilde{r}^D_x / \tilde{r}^D_y$ at $\alpha_s = 10^4$ and $\mu_m / \mu_0 = 1.04$.

The far-right column in Figure 7 shows that diamagnetic ellipsoids with different aspect ratios display rotational symmetry around a paramagnetic sphere at high medium permeabilities. In particular, the assembly of diamagnetic spheres around a paramagnetic sphere shows a rotational symmetry at high medium permeabilities, which agrees with previously reported experiments.[27] Furthermore, diamagnetic ellipsoids ($2 \leq \tilde{r}^D_x / \tilde{r}^D_y \leq 4$) assemble into structures with rotational symmetry, where the minimum axis of the ellipsoids is normal to the paramagnetic sphere. However, when $\tilde{r}^D_x / \tilde{r}^D_y = 5$, entropic interactions overcome dipolar interactions, and the rotational symmetry breaks down due to the geometry frustration of the ellipsoids around the sphere's perimeter.

Besides, Figure 7 shows that the rotational symmetry breaks down as the medium permeability decreases, promoting multilayer structures around the paramagnetic sphere, which results in an opposite trend as the previous results shown in Figure 6. Low medium permeabilities promote weak dipolar interaction between diamagnetic particles (Figure 4(b)), allowing them to form packing arrangements around the paramagnetic sphere. In particular, due to geometric frustration, the minimum axis of the ellipsoids ($\tilde{r}^D_x / \tilde{r}^D_y > 1$) is tilted with respect to the normal vector to the paramagnetic sphere, forming left or right-handed vortex structures, and symmetric structures centered at the paramagnetic sphere. The symmetry breaking of the structures becomes more apparent as the aspect ratio of the diamagnetic ellipsoids increases, where the diamagnetic ellipsoids form multilayer structures with no predefined alignment of the ellipsoids around the paramagnetic sphere.

3.5 Binary enclosed structures

In this section, we analyze the conditions in which diamagnetic (satellite) particles form enclosed structures around a paramagnetic sphere at $\alpha_s = 10^4$. We will analyze the impact of dipolar interactions on the structures in the next section. Figures 8 - 9 show the snapshots of MC simulations of the directed assembly of a paramagnetic sphere with different radii $\tilde{r}^P$ and diamagnetic ellipsoids with different aspect ratios $\tilde{r}^D_x / \tilde{r}^D_y$. The
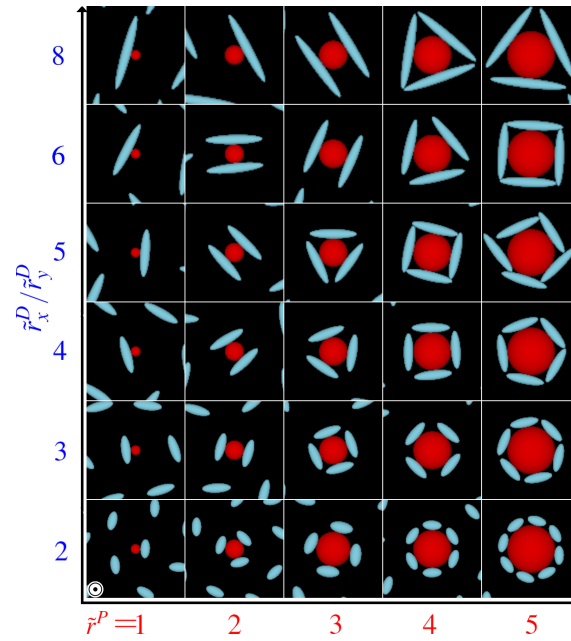
Fig. 9 Snapshots of the Monte Carlo simulations of the directed assembly of binary suspensions composed of a paramagnetic sphere (red) with radius $\tilde{r}^P$ and diamagnetic ellipsoids (cyan) with different aspect ratios $\tilde{r}_x^D/\tilde{r}_y^D$ at $\alpha_s = 10^4$ and $\mu_m/\mu_0 = 1.26$.

relative medium permeability is $\mu_m/\mu_0 = 1.04$ in Figure 8 and $\mu_m/\mu_0 = 1.26$ in Figure 9. Furthermore, Figures S4-S5 show the radial distribution function $g(\tilde{r})$ for different conditions analyzed in this section.

Figure 8 ($\mu_m/\mu_0 = 1.04$) shows diamagnetic ellipsoids form a single particle enclosure under the following conditions. The first one is when the radius of the paramagnetic particle is smaller or equal to the minimum axis of the diamagnetic ellipsoids ($\tilde{r}^P = 1$ with $\tilde{r}_x^D/\tilde{r}_y^D = 2-3$). The second condition is when the diamagnetic ellipsoids do not reach their maximum packing around the paramagnetic sphere, as shown in $\tilde{r}^P = 2$ with $\tilde{r}_x^D/\tilde{r}_y^D = 4-5$. Results suggest the enclosed structures are correlated with the effective length of the dipolar interaction that reaches only a few particle radii (Figure 4). However, the length of the dipolar interaction increases as the radius $\tilde{r}^P$ of the paramagnetic sphere increases, which generates multilayer structures of diamagnetic ellipsoids around the sphere, as explained in the previous section. However, the condition of a particle enclosure fails for higher aspect ratios, where only two diamagnetic ellipsoids attach to the paramagnetic sphere.

Figure 9 shows structures with a defined rotational symmetry at different combinations of a paramagnetic sphere and diamagnetic ellipsoids at a high medium permeability ($\mu_m/\mu_0 = 1.26$). As previously explained, the repulsive dipolar interaction between the diamagnetic particles increases at high medium permeabilities, which limits the arrangement of particles to a monolayer with different rotational symmetries. Simulation results in Figure 9 show that varying the sphere radius and ellipsoid aspect ratio tunes the entropic and the dipolar interactions, promoting open and close-packed structures. The diamagnetic ellipsoids form open-packed structures if the assembled structure does not reach the maximum packing around the sphere. However, the diamagnetic ellipsoids form close-packed structures once the maximum packing is reached. In both structures, the assembly of diamagnetic ellipsoids forms structures with rotational symmetry around the paramagnetic sphere. The ellipsoids lose their rotational symmetry around the paramagnetic sphere if the assembly of diamagnetic ellipsoids is greater than the perimeter of the paramagnetic sphere. Figure 9 shows a limit in the

paramagnetic radius $(\tilde{r}^P)$ to promote enclosed structures of diamagnetic ellipsoids with rotational symmetry around the paramagnetic sphere. In a future contribution, we will explore different equilibrium phases, the threshold between open and enclosed structures, and their correlation with competing entropic and dipolar interactions.

3.6 Effect of the dipolar interactions

In this section, we analyze the effect of the dipolar interactions on the assembly of small structures. The dipole-dipole interaction parameter β is modified by changing the dipole-field interaction parameter α_s, as described in Eq. (27). Figure 10 shows the radial distribution function $g(\tilde{r})$ at different values of α_s for representative cases depicted in Figures 6 – 9. We focus the analysis on the relevant region to analyze selected
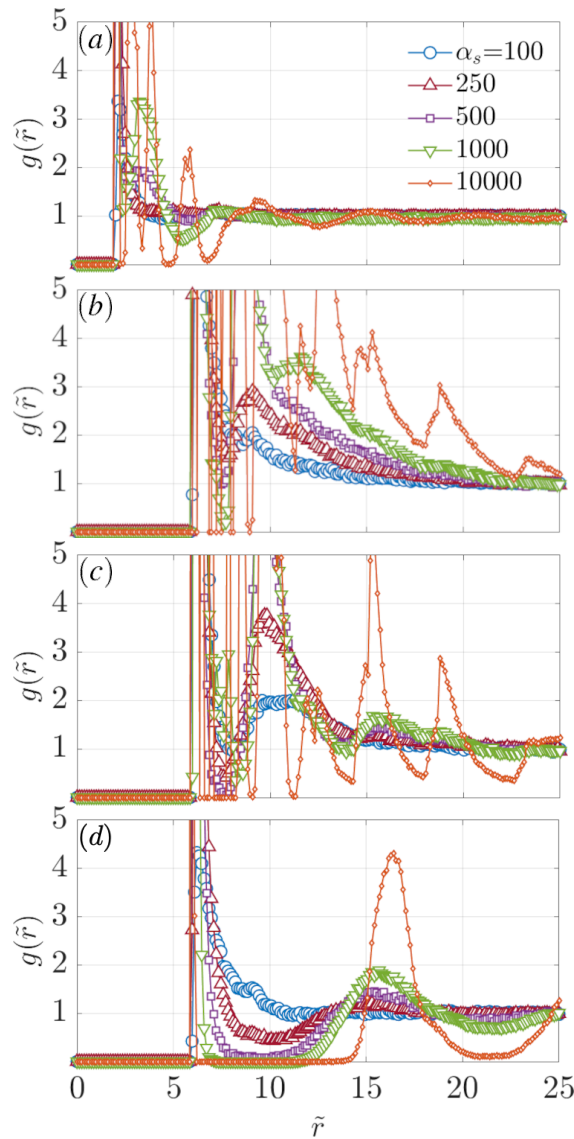

Fig. 10 Radial distribution function $g(\tilde{r})$ between the central diamagnetic particle and surrounding paramagnetic particles for different dipole-field interaction parameters α_s. (a) A central diamagnetic ellipsoid $(\tilde{r}_x^D/\tilde{r}_y^D = 6)$ and satellite paramagnetic spheres $(\tilde{r}^P = 1)$ at $\mu_m/\mu_0 = 1.11$, (b) − (d) a central paramagnetic sphere $(\tilde{r}^P = 5)$ and satellite diamagnetic ellipsoids $(\tilde{r}_x^D/\tilde{r}_y^D = 4)$ at (b) $\mu_m/\mu_0 = 1.04$, (c) $\mu_m/\mu_0 = 1.11$, and (d) $\mu_m/\mu_0 = 1.26$.

cases. However, Figures S3 – S6 (Supplementary information) show the full radial distribution function at different α_s values for every case analyzed in Figures 6 – 9. In general, the dipolar interaction affects the assembly of small structures in two main features: First, by promoting multilayers when dipolar interaction between satellite particles is small, and second, by forming single enclosures at high dipolar interactions.

Figure 10(a) shows the radial distribution function at different values of α_s for the assembly of a central diamagnetic ellipsoid with aspect ratio $\tilde{r}_x^D/\tilde{r}_y^D = 6$ and satellite paramagnetic spheres ($\tilde{r}^P = 1$) at a relative permeability of $\mu_m/\mu_0 = 1.11$ (See Figure 6). As the dipolar interaction increases, multiple peaks appear in $g(\tilde{r})$ at radii smaller than the major semi-axis of the ellipsoid ($\tilde{r} < 6$), indicating the assembly of paramagnetic spheres along the sides of the diamagnetic ellipsoid. Figure S3 shows a similar $g(\tilde{r})$ pattern in the other conditions analyzed in Figure 6 as α_s increases. Furthermore, Figure S3 shows peaks on $g(\tilde{r})$ at long distances from the central diamagnetic ellipsoid, which is correlated with the increasing dipolar interaction between surrounding paramagnetic spheres as the medium permeability decreases, see top panel of Figure 6.

Figures 10(b) – (d) show $g(\tilde{r})$ at different α_s values for the assembly of a central paramagnetic sphere with $\tilde{r}^P = 5$ and satellite diamagnetic ellipsoids with aspect ratio $\tilde{r}_x^D/\tilde{r}_y^D = 4$ at a relative permeability μ_m/μ_0 of (b) 1.04, (c) 1.11, and (d) 1.26 (See Figures 7 – 9). The second peak on $g(\tilde{r})$ at low α_s values spaces out the first peaks as the medium permeability increases due to the increasing dipolar interaction between the diamagnetic ellipsoids. Furthermore, results show multiple peaks within the range of interaction of the central paramagnetic sphere, as shown in Figures 10(b) – (c). The peaks are correlated with the formation of multilayers of diamagnetic ellipsoids around the sphere, as shown in Figures 7 – 8. Contrary, Figure 10(d) shows the first peak on $g(\tilde{r})$ becomes sharper as α_s increases, which is reflected in the formation of a monolayer of ellipsoids around the paramagnetic sphere, as shown in Figures 7 and 9.

4   Discussion

The induced dipole-dipole interaction energy quantified using the ellipsoid-dipole model in Eq. (25) shows a dependence in position by the tensor $\mathscr{G}$ and orientation by the rotation transformation matrix A^{JI}. The ellipsoid-dipole model includes the effect of shape anisotropy on the tensor $\mathscr{G}$, which is missing in the point-dipole model. Moreover, the induced dipole-dipole interaction between magnetizable particles has a similar dependence as the dipolar interaction between permanently magnetized particles.[48] Therefore, Eq. (25) applies to interacting magnetizable ellipsoids with different aspect ratios and material properties, as shown in Figures 6 - 9.

The presence of the magnetic nanoparticles in the ferrofluid medium might generate a slight deviation in the excluded volume, which is negligible due to the nanoparticle size being at least three orders of magnitude smaller than the micron-size ellipsoids used in the analysis. However, the rotational symmetry on the simulation results for binary suspensions composed of paramagnetic spheres around the central diamagnetic sphere (Figure 5) shows a similar phenomenological behavior as a function of the medium permeability of previously reported experiments.[27,28] The results show that the pairwise interaction energy between ellipsoids is a good approximation without considering the excluded volume effect of the magnetic nanoparticles in the system. Previously reported experiments show the assembly of colloidal superstructures of paramagnetic and diamagnetic micron-sized spheres form structures with a rotational symmetry around the central particle as shown in Figure 1 of Ref.[28]. However, we did not find other experimental results reporting the assembly of binary suspensions composed of magnetizable particles to validate the theoretical predictions using the ellipsoid-dipole model. Numerical results show a large variety of assembled structures composed of binary

ellipsoids by varying the particle aspect ratio and medium permeability, which alters the Clausius-Mossotti factor and the dipolar interaction between particles. The results in this study justify further experiments to complement previous analyses that show the equilibrium configurations of monodisperse magnetizable and polarizable particles,[26,53,55] as well as binary suspensions composed of particles with different aspect ratios and material properties.[13]

Many numerical results focus on the entropic interactions between hard anisotropic particles,[71,72,84–94] but equilibrium structures of magnetic anisotropic particles depend on both dipolar and entropic interactions.[34,48] We qualitatively describe the rotational symmetry of assembled structures to analyze competing entropic and dipolar interactions and their dependence on particle aspect ratio, size, and medium permeabilities. Our simulation results show enclosed structures with rotational symmetry at high medium permeabilities and structures with broken symmetry at low medium permeabilities due to the competition between interactions. However, the large variability of these structures requires further analysis to quantify the order parameters and transition conditions between open and enclosed structures, as well as the transition between structures with different rotational symmetries.

The dipolar interaction energy (Eq. (21)) evaluated using the ellipsoid-dipole model (Eq. (13)) is valid for magnetizable ellipsoids with different aspect ratios and material properties. The ellipsoid-dipole model results from the analytical solution of the ellipsoid under the influence of a uniform magnetic field,[63] and it's not valid for other particle shapes with no quadratic surface representation.[65] New models or extensions for the Clausius-Mossotti factor (Eq. (11)) and the $\mathscr{G}$ tensor (Eq. (14)) are necessary to quantify the assembly of structures composed of other particle shapes, such as superballs and superellipsoids.[77,95–97]

5   Conclusions

We report a closed-form analytical expression, the ellipsoid-dipole model, to quantify the dipolar interaction between magnetizable ellipsoids with different aspect ratios and material properties as a function of position and orientation. We analyze the directed assembly of binary suspensions composed of paramagnetic and diamagnetic ellipsoids in a ferrofluid medium with different permeabilities. The simulation results show that particle aspect ratio, size, and particle/medium permeabilities tune the rotational symmetry and packing order of the assembled binary structures. The aspect ratio of the diamagnetic (central) particle breaks the orientational symmetry of the structures compared with the suspensions of binary spheres. Moreover, the rotational symmetry decreases as the aspect ratio of the diamagnetic (central) particles increases. Conversely, the simulation results show that when the difference between diamagnetic particle permeability and medium permeability is small, the weak repulsive interaction between diamagnetic (satellite) particles promotes aggregation without orientational symmetry. Furthermore, the dipolar interaction promotes enclosed particle structures with rotational symmetry when there is a significant difference between diamagnetic particle permeability and medium permeability, *i.e.*, for a strong dipolar interaction between satellite particles. However, the relative size between particles tunes the competing entropic and dipolar interactions, promoting assembled enclosure formation with broken rotational symmetry.

Conflicts of interest

There are no conflicts to declare.

Data availability

The data supporting this article is included as part of the Supplementary Information.

Acknowledgements

Notes and references

1 K. J. Lee, J. Yoon and J. Lahann, *Current Opinion in Colloid & Interface Science*, 2011, **16**, 195–202.

2 P. Tierno, *Phys. Chem. Chem. Phys.*, 2014, **16**, 23515–23528.

3 B. M. Teo, D. J. Young and X. J. Loh, *Particle & Particle Systems Characterization*, 2016, **33**, 709–728.

4 J. M. Meijer and L. Rossi, *Soft Matter*, 2021, **17**, 2354–2368.

5 Z. Ma, J. Mohapatra, K. Wei, J. P. Liu and S. Sun, *Chemical Reviews*, 2023, **123**, 3904–3943.

6 H. Xie, M. Sun, X. Fan, Z. Lin, W. Chen, L. Wang, L. Dong and Q. He, *Science Robotics*, 2019, **4**, eaav8006.

7 Q. Wang, K. F. Chan, K. Schweizer, X. Du, D. Jin, S. C. H. Yu, B. J. Nelson and L. Zhang, *Science Advances*, 2021, **7**, eabe5914.

8 B. Li, D. Zhou and Y. Han, *Nature Reviews Materials*, 2016, **1**, 15011.

9 H. Massana-Cid, F. Meng, D. Matsunaga, R. Golestanian and P. Tierno, *Nature Communications*, 2019, **10**, 2444.

10 R. S. Hendley, L. Zhang and M. A. Bevan, *ACS Nano*, 2023, **17**, 20512–20524.

11 J. A. Champion, Y. K. Katare and S. Mitragotri, *Journal of Controlled Release*, 2007, **121**, 3–9.

12 J. A. Champion and S. Mitragotri, *Pharmaceutical Research*, 2009, **26**, 244–249.

13 A. F. Demirörs, F. Eichenseher, M. J. Loessner and A. Studart, *Nature Communications*, 2017, **8**, 1872.

14 J. D. Forster, J.-G. Park, M. Mittal, H. Noh, C. F. Schreck, C. S. O'Hern, H. Cao, E. M. Furst and E. R. Dufresne, *ACS Nano*, 2011, **5**, 6695–6700.

15 Q. Zhang, M. Janner, L. He, M. Wang, Y. Hu, Y. Lu and Y. Yin, *Nano Letters*, 2013, **13**, 1770–1775.

16 M. Wang, L. He, W. Xu, X. Wang and Y. Yin, *Angewandte Chemie International Edition*, 2015, **54**, 7077–7081.

17 Z. Li, C. Qian, W. Xu, C. Zhu and Y. Yin, *Science Advances*, 2021, **7**, eabh1289.

18 Z. Huang, Y. Zhu, J. Zhang and G. Yin, *The Journal of Physical Chemistry C*, 2007, **111**, 6821–6825.

19 S. Srinivasan, V. Praveen, R. Philip and A. Ajayaghosh, *Angewandte Chemie International Edition*, 2008, **47**, 5750–5754.

20 S. Parvate, P. Dixit and S. Chattopadhyay, *The Journal of Physical Chemistry B*, 2020, **124**, 1323–1360.

21 S. C. Glotzer and M. J. Solomon, *Nature Materials*, 2007, **6**, 557–562.

22 M. Grzelczak, J. Vermant, E. M. Furst and L. M. Liz-Marzán, *ACS Nano*, 2010, **4**, 3591–3605.

23 M. J. Solomon, *Current Opinion in Colloid & Interface Science*, 2011, **16**, 158–167.

24 B. Bharti and O. D. Velev, *Langmuir*, 2015, **31**, 7897–7908.

25 *Anisotropic Particle Assemblies*, ed. N. Wu, D. Lee and A. Striolo, Elsevier, Amsterdam, 2018, pp. i–ii.

26 R. S. Hendley, I. Torres-Díaz and M. A. Bevan, *Soft Matter*, 2021, **17**, 9066–9077.

27 R. M. Erb, H. S. Son, B. Samanta, V. M. Rotello and B. B. Yellen, *Nature*, 2009, **457**, 999–1002.

28 K. H. Li and B. B. Yellen, *Applied Physics Letters*, 2010, **97**, 083105.

29 S. D. Peroukidis, K. Lichtner and S. H. L. Klapp, *Soft Matter*, 2015, **11**, 5999–6008.

30 Z. M. Sherman and J. W. Swan, *ACS Nano*, 2016, **10**, 5260–5271.

31 Z. M. Sherman, D. Ghosh and J. W. Swan, *Langmuir*, 2018, **34**, 7117–7134.

32 V. Hakonsen, G. Singh, J. A. De Toro, P. S. Normile, E. Wahlström, J. He and Z. Zhang, *Advanced Science*, 2021, **8**, 2002683.

33 R. W. Chantrell, A. Bradbury, J. Popplewell and S. W. Charles, *Journal of Applied Physics*, 1982, **53**, 2742–2744.

34 L. Rossi, J. G. Donaldson, J.-M. Meijer, A. V. Petukhov, D. Kleckner, S. S. Kantorovich, W. T. M. Irvine, A. P. Philipse and S. Sacanna, *Soft Matter*, 2018, **14**, 1080–1087.

35 F. Martinez-Pedrero, A. Cebers and P. Tierno, *Phys. Rev. Appl.*, 2016, **6**, 034002.

36 F. Martinez-Pedrero, A. Cebers and P. Tierno, *Soft Matter*, 2016, **12**, 3688–3695.

37 S. Kantorovich, E. Pyanzina and F. Sciortino, *Soft Matter*, 2013, **9**, 6594–6603.

38 R. D. Stoy, *Journal of Applied Physics*, 1989, **66**, 5093–5095.

39 R. D. Stoy, *Journal of Applied Physics*, 1989, **65**, 2611–2615.

40 T. B. Jones, *Electromechanics of Particles*, Cambridge University Press, 1995.

41 E. M. Furst and A. P. Gast, *Phys. Rev. E*, 2000, **62**, 6916–6925.

42 J. Faraudo, J. S. Andreu, C. Calero and J. Camacho, *Advanced Functional Materials*, 2016, **26**, 3837–3858.

43 X. Fan and A. Walther, *Chem. Soc. Rev.*, 2022, **51**, 4023–4074.

44 H. König, R. Hund, K. Zahn and G. Maret, *European Physical Journal E – Soft Matter*, 2005, **18**, 287–293.

45 R. M. Lahcen Assoud and H. Löwen, *Molecular Physics*, 2011, **109**, 1385–1391.

46 M. Wang, L. He and Y. Yin, *Materials Today*, 2013, **16**, 110–116.

47 V. Malik, A. Pal, O. Pravaz, J. J. Crassous, S. Granville, B. Grobety, A. M. Hirt, H. Dietsch and P. Schurtenberger, *Nanoscale*, 2017, **9**, 14405–14413.

48 T. Thelen, A. Jara and I. Torres-Díaz, *Soft Matter*, 2023, **19**, 640–651.

49 J. Mohapatra, M. Xing, J. Elkins, J. Beatty and J. P. Liu, *Advanced Functional Materials*, 2021, **31**, 2010157.

50 Q. Fan, Z. Li, C. Wu and Y. Yin, *Precision Chemistry*, 2023, **1**, 272–298.

51 A. Pal, C. A. De Filippo, T. Ito, M. A. Kamal, A. V. Petukhov, C. De Michele and P. Schurtenberger, *ACS Nano*, 2022, **16**, 2558–2568.

52 T. Troppenz, A. Kuijk, A. Imhof, A. van Blaaderen, M. Dijkstra and R. van Roij, *Phys. Chem. Chem. Phys.*, 2015, **17**, 22423–22430.

53 A. Kuijk, T. Troppenz, L. Filion, A. Imhof, R. van Roij, M. Dijkstra and A. van Blaaderen, *Soft Matter*, 2014, **10**, 6249–6255.

54 Y. Yang, L. Gao, G. P. Lopez and B. B. Yellen, *ACS Nano*, 2013, **7**, 2705–2716.

55 J. J. Crassous, A. M. Mihut, E. Wernersson, P. Pfleiderer, J. Vermant, P. Linse and P. Schurtenberger, *Nature Communications*, 2014, **5**, 5516.

56 M. Rotunno, T. Bellini, Y. Lansac and M. A. Glaser, *The Journal of Chemical Physics*, 2004, **121**, 5541–5549.

57 C. W. Shields IV, S. Zhu, Y. Yang, B. Bharti, J. Liu, B. B. Yellen, O. D. Velev and G. P. López, *Soft Matter*, 2013, **9**, 9219–9229.

58 D. Du, P. He, Y. Zeng and S. L. Biswal, *Journal of Magnetism and Magnetic Materials*, 2016, **417**, 100–105.

59 R. Zhou, C. A. Sobecki, J. Zhang, Y. Zhang and C. Wang, *Phys. Rev. Appl.*, 2017, **8**, 024019.

60 C. A. Sobecki, J. Zhang, Y. Zhang and C. Wang, *Phys. Rev. Fluids*, 2018, **3**, 084201.

61 C. Sobecki, J. Zhang and C. Wang, *Micromachines*, 2020, **11**, 1–24.

62 J. Zhang, R. Zhou and C. Wang, *Journal of Micromechanics and Microengineering*, 2019, **29**, 104002.

63 J. A. Stratton, *Electromagnetic Theory*, McGraw-Hill Book Company, Inc., New York, 1941, p. 615.

64 V. Denner and H. A. Pohl, *Journal of Electrostatics*, 1982, **13**, 167–174.

65 J. C. Maxwell, *A Treatise on Electricity and Magnetism: vol. 2*, Dover Publications, 1873.

66 N. G. Green and T. B. Jones, *Journal of Physics D: Applied Physics*, 2006, **40**, 78.

67 N. Metropolis and S. Ulam, *Journal of the American Statistical Association*, 1949, **44**, 335–341.

68 M. P. Allen and D. J. Tildesley, *Computer Simulation of Liquids*, Oxford University Press, 2017.

69 D. Frenkel and B. Smith, *Understanding Molecular Simulations: from Algorithms to Applications*, Academic Press, 2023.

70 J. M. Kosterlitz and D. J. Thouless, *Journal of Physics C: Solid State Physics*, 1972, **5**, L124.

71 G. Odriozola, *The Journal of Chemical Physics*, 2009, **131**, 144107.

72 G. Odriozola, *The Journal of Chemical Physics*, 2012, **136**, 134505.

73 D. J. Evans, *Molecular Physics*, 1977, **34**, 317–325.

74 D. J. Evans and S. Murad, *Molecular Physics*, 1977, **34**, 327–331.

75 H. Morgan and N. G. Green, *AC electrokinetics : colloids and nanoparticles*, Institute of Physics Pub., Philadelphia, Pa., 2003.

76 I. Torres-Díaz, R. S. Hendley, A. Mishra, A. J. Yeh and M. A. Bevan, *Soft Matter*, 2022, **18**, 1319–1330.

77 I. Torres-Díaz and M. A. Bevan, *Langmuir*, 2017, **33**, 4356–4365.

78 R. Rosensweig, *Ferrohydrodynamics*, Dover Publications, 2013.

79 D. T. Grob, N. Wise, O. Oduwole and S. Sheard, *Journal of Magnetism and Magnetic Materials*, 2018, **452**, 134–140.

80 P. Li, D. Kilinc, Y.-F. Ran and G. U. Lee, *Lab Chip*, 2013, **13**, 4400–4408.

81 B. Sinha, S. Anandakumar, S. Oh and C. Kim, *Sensors and Actuators A: Physical*, 2012, **182**, 34–40.

82 G. Fonnum, C. Johansson, A. Molteberg, S. Mørup and E. Aksnes, *Journal of Magnetism and Magnetic Materials*, 2005, **293**, 41–47.

83 M. D. Tarn, S. A. Peyman, D. Robert, A. Iles, C. Wilhelm and N. Pamme, *Journal of Magnetism and Magnetic Materials*, 2009, **321**, 4115–4122.

84 D. Frenkel and B. Mulder, *Molecular Physics*, 1985, **55**, 1171–1192.

85 P. F. Damasceno, M. Engel and S. C. Glotzer, *ACS Nano*, 2012, **6**, 609–614.

86 S. Torquato and Y. Jiao, *Phys. Rev. E*, 2012, **86**, 011102.

87 G. Cinacchi and S. Torquato, *The Journal of Chemical Physics*, 2015, **143**, 224506.

88 V. N. Manoharan, *Science*, 2015, **349**, 1253751.

89 C. Avendaño and F. A. Escobedo, *Current Opinion in Colloid & Interface Science*, 2017, **30**, 62–69.

90 R. K. Cersonsky, G. van Anders, P. M. Dodd and S. C. Glotzer, *Proceedings of the National Academy of Sciences*, 2018, **115**, 1439–1444.

91 E. S. Harper, G. van Anders and S. C. Glotzer, *Proceedings of the National Academy of Sciences*, 2019, **116**, 16703–16710.

92 C. Fernández-Rico, M. Chiappini, T. Yanagishima, H. de Sousa, D. G. A. L. Aarts, M. Dijkstra and R. P. A. Dullens, *Science*, 2020, **369**, 950–955.

93 C. Hou, L. Gao, Y. Wang and L.-T. Yan, *Nanoscale Horiz.*, 2022, **7**, 1016–1028.

94 S. Lee, T. Vo and S. C. Glotzer, *Nature Chemistry*, 2023, **15**, 905–912.

95 Y. Jiao, F. H. Stillinger and S. Torquato, *Phys. Rev. E*, 2009, **79**, 041309.

96 G. W. Delaney and P. W. Cleary, *Europhysics Letters*, 2010, **89**, 34002.

97 Y. Yuan, K. VanderWerf, M. D. Shattuck and C. S. O'Hern, *Soft Matter*, 2019, **15**, 9751–9761.

"The data supporting this article is included as part of the Supplementary Information."